scientific reports

Check for updates

OPEN

Topological edge state resonance as gamma dosimeter using poly nanocomposite in symmetrical periodic structure

Zaky A. Zaky[1,2,3]✉, Mohammed Sallah[4], V. D. Zhaketov[3,5] & Arafa H. Aly[1]

Topological edge state resonance based sensor, including photonic crystal, is proposed for gamma radiation detection. This article initiates by showing the fundamental principles of photonic crystal, topological edge state, and gamma dosimeter, highlighting their benefits and performance over conventional detectors. This study discusses the possibility of exciting a topological edge state resonance using two symmetrical photonic crystals composed of silicon doped with poly(ethylene oxide) nanocomposite as a gamma detector. The simulation results using the transfer matrix method recorded a sensitivity of 1.24 nm/Gy for gamma doses from 0 to 100 Gy and 0.34 nm/Gy for gamma doses from 100 to 200 Gy when the proposed structure is composed of silicon doped with poly(ethylene oxide) nanocomposite as an active material. It is found that the maximum figure of merit and quality factor of the detector are $6.04 \times 10^3\ \mathrm{Gy}^{-1}$ and 1.30×10^7, respectively. Thus, this innovative topological edge state resonance-based detector is extremely promising for radiation detection. According to these investigations, topological edge state gamma sensors have distinct advantages over traditional dosimeters in terms of increased sensitivity, robustness against disorder, and simplified structure, which makes them appropriate for use in environmental radiation monitoring and medical imaging.

Keywords Periodic structure, Polymer nanocomposite, Gamma radiation, Dosimeter, Topological edge state

Photonic crystals, or PhCs, are periodic structures that have attracted much attention lately because of their remarkable nanoscale light control and manipulation capabilities[1,2]. PhCs, which consist of materials with high and low dielectric constants or refractive indices (RIs), display distinct optical characteristics such as photonic bandgaps (PBG) and robust electromagnetic wave (EMW) confinement[3,4]. PBG in PhCs is due to the multiple Bragg scattering in periodic structures. Wavelengths of EMW within PBG range cannot propagate. Advances in the theoretical knowledge and production processes of PhCs have resulted in significant improvements in a variety of devices and applications, such as smart windows[5], sensors[6–9], etc. PhCs have shown great promise for next-generation sensing devices[10,11].

One-dimensional PhC (1DPhC) features a periodic configuration of high and low RI materials running along their length and is widely used in different structures. By tailoring the composition and geometry of the 1DPhC, remarkable improvements have been achieved in sensing applications. Topological 1DPhC configurations possess features such as integrated optical systems and can be ultra-compact using an easy-to-manufacture method[12,13]. The first topological PhCs were suggested theoretically by Raghu and Haldane in 2008[14,15]. The ability of topological PhCs to solve the issue of energy loss in PhC systems due to manufacturing processes is one of the most important benefits. Several new phenomena have been seen in PhCs since topology was introduced, such as topological edge state (TES). TES is a confinement of specific wavelengths of EMW at the interface between two identical or different PhCs. 1DPhCs are commonly utilized for manufacturing TES modes because 2DPhCs and 3DPhCs are more complicated to fabricate[15]. Gao et al.[16] experimentally and theoretically proposed a coupling between the Fabry–Pérot cavity mode and TES in the form of Fano resonance using three 1D PhCs.

[1]TH-PPM Group, Physics Department, Faculty of Sciences, Beni-Suef University, Beni Suef 62514, Egypt. [2]Academy of Scientific Research and Technology (ASRT), Cairo, Egypt. [3]Frank Laboratory of Neutron Physics, Joint Institute for Nuclear Research, Dubna, Russia141980. [4]Department of Physics, College of Sciences, University of Bisha, P.O. Box 344, 61922 Bisha, Saudi Arabia. [5]Moscow Institute of Physics and Technology (State University), Dolgoprudnyi, Moscow Oblast, Russia. ✉email: zaky.a.zaky@science.bsu.edu.eg

Porous silicon (PSi) attracted growing interest in various fields and PhC configurations because of its high sensitivity (S) and extensive surface area[17–19]. The technology for preparing PSi is among the fastest and simplest methods for producing PhCs[17,18]. Zaky et al.[20] designed a sensor with exceptional sensitivity using a CS-PhC of PSi. Zaky et al.[21] proposed a CS-PhC to detect gamma radiation using PSi doped with a DPV polymer. Polymer nanocomposites (PNCs) have developed into promising energy conversion and storage application materials because of their great thermal and mechanical stability, excellent ionic conductivity, and broad stability. PNC has garnered increased interest as a sensitive material for various emerging fields, including supercapacitors, batteries, radiation detectors, and fuel cells, due to its low-cost and flexibility[22–26]. Indigo dye samples were used to detect radiation with $S = 0.0002$ nm/Gy by Bich et al.[27]. Quantum dot/PNCs have shown significant potential for high-performance, low-cost spectroscopic gamma detectors[28]. Gadolinium oxide-PNCs recorded high-resolution for gamma detection[29]. Conductive PNCs were designed as real-time GRD and exhibited significant enhancement for efficient gamma ray harvesting systems[30].

In this study, according to our knowledge, TES resonance using 1DPhCs is proposed as gamma radiation detection for the first time. Poly(ethylene oxide) nanocomposite (PEONC) is used as a sensitive material for gamma doses. The experimental RIs of PEONC at different irradiation doses are fitted[26]. The effect of porosity (ratio of PEONC in PSi layers), and number of periods are investigated to attain superior results.

Theoretical model and basic equations

Figure 1 represents a schematic figure of two symmetrical PhCs (PhC1 and PhC2) composed of silicon doped with PEONC as a gamma detector as $\left[\text{Air} * (\text{HL})^N (\text{LH})^N * \text{Substrate}\right]$. Layers H and L are PSi and Al_2O_3, respectively. The thicknesses H and L are 200 nm and 120 nm, respectively. PSi layer is doped with 10% PEONC as an active material for gamma radiation. Both PhC1 and PhC2 are repeated for N times ($N = 5$). The EMWs will normally incident on the structure ($\theta = 0$) from the air. The RIs of air and substrate are 1 and 1.52, respectively.

The RIs of Al_2O_3 according to Sellmeier equation by fitting the experimental data in Ref.[31], and PSi according to Bruggeman's effective equations[32] can be calculated as follows (λ in μm):

$$n_{\text{Al2O3}} = -2.012168 + \frac{4.352187\lambda^2}{\lambda^2 - 0.045773^2} + \frac{0.117166\lambda^2}{\lambda^2 - 0.187027^2}. \tag{1}$$

$$\mathrm{n_{PSi}} = 0.5\sqrt{\psi + \sqrt{\psi^2 + 8\mathrm{n_{si}^2 n_{PEONC}^2}}},$$

$$\psi = 3\ \mathrm{P}\ \left(\mathrm{n_{PEONC}^2} - \mathrm{n_{si}^2}\right) + \left(2\mathrm{n_{si}^2} - \mathrm{n_{PEONC}^2}\right), \tag{2}$$

where P is the ratio of PEONC in PSi and $\mathrm{n_{Si}} = 3.7$. The final shape of PSi will be silicon doped with PEONC. So, the mechanical robustness will not be affected with porosity. In our study, the porosity refers to the PEONC, not air cavities. The RI of Si is slightly affected at high gamma doses up to 1000 kGy (less than 5×10^{-5})[33]. Besides, the thermo-optic coefficient of Si is very small (2.3×10^{-4}) at a gamma dose of 66.5 kGy and a temperature of 32 °C[33]. In 2018, Ahmed et al.[34] studied the effect of gamma radiation on Si-PhC devices using Monte Carlo codes. Ahmed et al.[34] found that thermo-optic coefficient, dispersion, characteristic group index, temperature sensitivity, peak width, and peak center remain constant for aggregate doses up to 1 MGy. For Al_2O_3, even at 46 KGy, the optical properties of it seem to be constant[31]. Si layers can be deposited on a substrate of Al_2O_3[35–39]. Besides, Al_2O_3 strips can be deposited on nanoporous Si[40]. Additionally, silicon doped with composites can be fabricated[41].

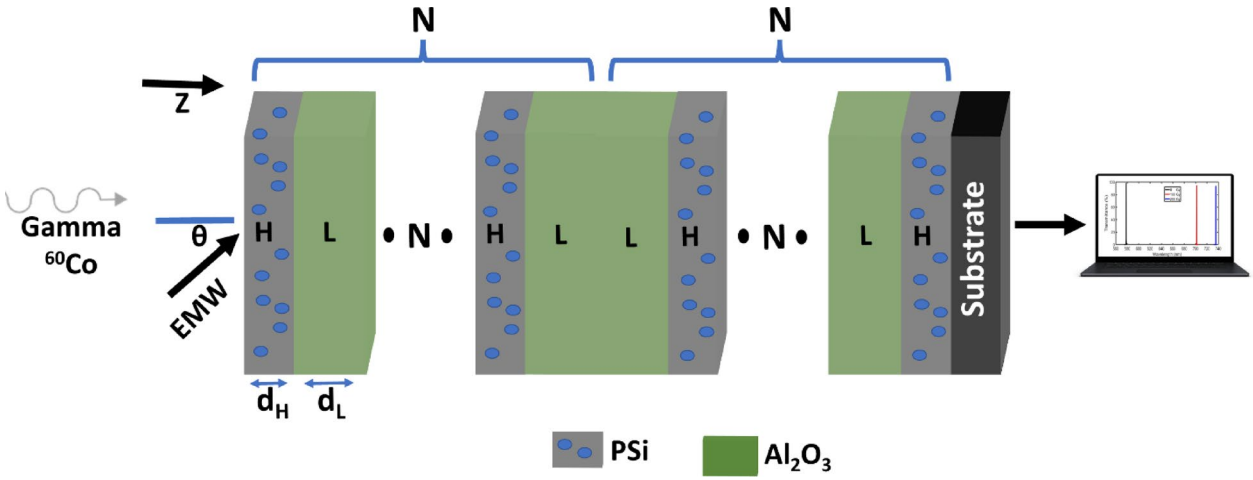

Fig. 1. Schematic design of symmetrical PhCs composed of silicon doped with PEONC.

The gamma radiation effect on Si and Al_2O_3 is neglected[31,42,43]. The PEONC's RI at different gamma doses is calculated as follows (300 nm $\leq \lambda \leq$ 800 nm, and λ should be in μm in equations)[26]:
At gamma dose of 0 Gy:

$$n_{\mathrm{PEONC}} = -50.99\lambda^3 + 109.7\lambda^2 - 78.54\lambda + 20.21. \tag{3}$$

At gamma dose of 100 Gy:

$$n_{\mathrm{PEONC}} = 1267.32\lambda^6 - 4530.09\lambda^5 + 6714.24\lambda^4 - 5289.53\lambda^3 + 2341.49\lambda^2 - 554.456\lambda + 61.5716. \tag{4}$$

At gamma dose of 200 Gy:

$$n_{\mathrm{PEONC}} = 41.43\lambda^4 - 101.9\lambda^3 + 93.13\lambda^2 - 37.84\lambda + 14.15. \tag{5}$$

Using MATLAB software, the transmittance (T) of EMWs (transverse electric) propagating through symmetrical PhCs composed of silicon doped with PEONC at different gamma irradiation doses is calculated using the transfer matrix method (TMM) as follows[44–55]:

$$T\,(\%) = 100 \times \frac{p_s}{p_0} ?t?^2, \tag{6}$$

where

$$t = \frac{2p_0}{(A_{11} + A_{12}p_s)\,p_0 + (A_{21} + A_{22}p_s)}, \tag{7}$$

$$\begin{vmatrix} A_{11} & A_{12} \\ A_{21} & A_{22} \end{vmatrix} = (a_H a_L)^N (a_L a_H)^N, \tag{8}$$

$$p_i = n_i cos\,(\theta_i)\,, \tag{9}$$

where $i = 0$(for air), H(for PSi), L(for Al_2O_3), and s (for substrate).

$$a_H = \begin{bmatrix} cos\sigma_H & \left(-\frac{i}{p_H}\right) sin\sigma_H \\ -ip_H sin\sigma_H & cos\sigma_H \end{bmatrix}, \tag{10}$$

$$a_L = \begin{bmatrix} cos\sigma_L & \left(-\frac{i}{p_L}\right) sin\sigma_L \\ -ip_L sin\sigma_L & cos\sigma_L \end{bmatrix}, \tag{11}$$

$$\sigma_H = \frac{2\pi}{\lambda} d_H n_H cos\theta_H \tag{12}$$

$$\sigma_L = \frac{2\pi}{\lambda} d_L n_L cos\theta_L \tag{13}$$

TMM has already been used in the construction of different filters[5], detectors[20,56–59], and other simulations. Wang et al.[60] practical and theoretical (using TMM) studied the 1D reflector's reflectance producing very good matching. Gutierrez et al.[61] fabricated and simulated (using TMM) a multi-use detector. The numerical and experimental results coincided.

Results and discussions

Figure 2A clear the RIs of PEONC at different gamma doses from 0 to 200 Gy. By increasing the gamma doses, RI of PEONC basically increases due to breaking chains. This chain breaking causes some changes like H_2 releasing, cross-linking, O_2 absorption by carbon, energy gap reduction, formation of interband states, and the RI increase[62,63]. This inverse behavior energy gap and RI are consistent with the Penn model[64]. RIs of PSi (P = 10%) doped with PEONC at different gamma doses from 0 to 200 Gy are represented in Fig. 2B. According to Eqs. (2) and (3), by irradiating the doped PSi layers with gamma doses, the RIs of doped PSi increase significantly due to the increase of the RI of PEONC. Due to the stability of RIs of PSi at wavelengths of 550 nm $\leq \lambda \leq$ 800 nm, this range of wavelengths is recommended.

In the absence of gamma dose, there is a PBG in the transmittance spectra of one PhC (PhC1) due to the high contrast between the RIs of Al_2O_3 and PSi, as clear in Fig. 3A. The PBG has a left edge at 550 nm and a right edge at 622 nm. By studying the transmittance spectra of the symmetrical structure of PhC1* PhC2, an outstanding peak at a wavelength of 613.04 nm (inside the PBG) appeared. This outstanding peak is due to the localization of EMW at the interface between PhC1 and PhC2[48]. In Fig. 3B, by increasing gamma radiation from 0 to 100 Gy and 200 Gy, the outstanding peak position (λ_{TES}) is moved from 613. 04 to 668.83 nm, and 683.08 nm due to the RI increase, according to the standing wave relation:

$$m\lambda_d = n_{eff} D, \tag{14}$$

where m, n_{eff}, and D are integer, effective RI, and geometric path difference, respectively.

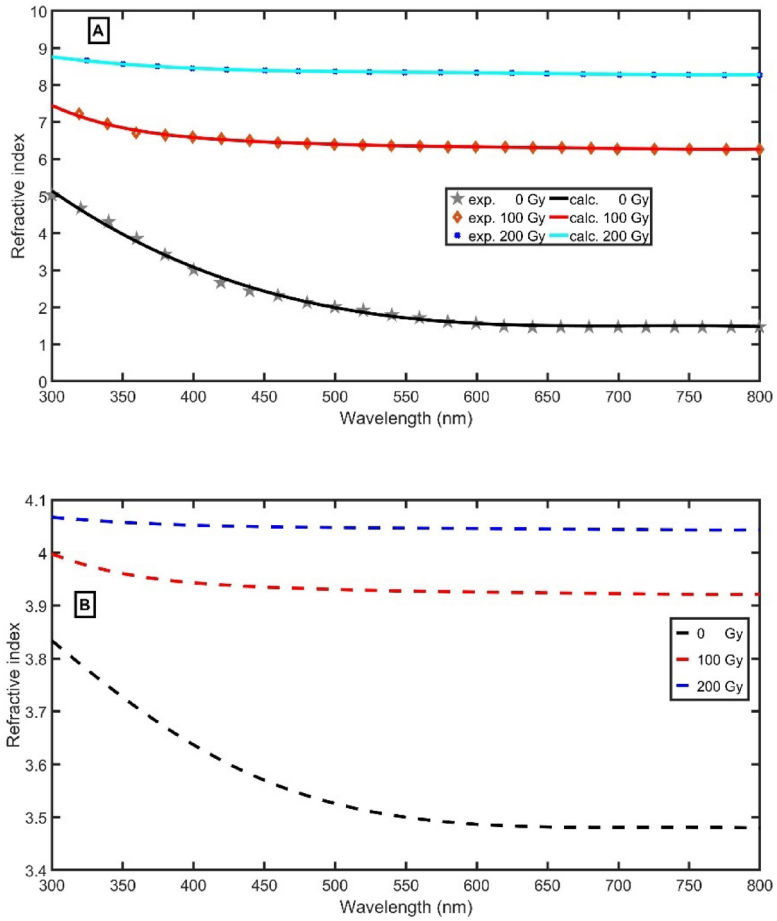

Fig. 2. (**A**) Measured[26] and our fitted RIs of PEONC, and (**B**) RIs of PSi ($P = 10\%$) doped with PEONC at different gamma doses from 0 to 200 Gy.

Any sensing device that has high S, narrow peaks with low bandwidth (FWHM), high figure of merit (FoM), high quality-factor (Q), and low detection limit (LoD) tends to perform better, as follows:

$$S = \frac{\Delta\lambda_{TES}}{\Delta\gamma}, \tag{15}$$

$$FoM = \frac{S}{FWHM}, \tag{16}$$

$$Q = \frac{\lambda_{TES}}{FWHM}\ , \tag{17}$$

$$LoD = \frac{\lambda_{TES}}{20SQ}. \tag{18}$$

As clear in Fig. 4, increasing the ratio of PEONC in PSi layers from 12 to 14%, 16%, 18%, 20%, and 22% widens the shift between outstanding peaks ($\Delta\lambda_{TES}$), and enhances the performance of the sensor. By increasing the ratio of PEONC in PSi layers from 10 to 12%, 14%, 16%, 18%, 20%, and 22%, the shift between outstanding peaks increases from 70.04 nm, 84.46 nm, 98.96 nm, 113.52 nm, 128.11 nm, 142.72 nm, and 157.3 nm. As clear in Fig. 4, at a gamma dose of 100 Gy and 200 Gy, a second PBG contains another outstanding peak (undesirable) in the wavelength range of concern. It is noticed that a second undesirable peak approaches the mean outstanding peak by increasing the porosity. At porosities higher than 22%, the undesirable peak overlaps with the mean outstanding peak. As a result, porosity of 22% is optimum porosity.

As clear in Fig. 5A, there is a high stability (97.5%) in the transmittance of outstanding TES peak at 0 Gy of gamma dose because of the high confinement of EMW at the interface between PhC1 and PhC2. The FWHM increases with PSi porosity due to moving the outstanding TES peak closer to the edge of the PBG. As the increase in PSi porosity widens the shift between outstanding peaks, the sensitivity gradually increases with PSi porosity, as clear in Fig. 5B. Besides, FoM varies between 1.25 and 1.42 Gy^{-1}. In Fig. 5C, the Q gradually decreases, and LoD decreases to a minimum value at $P = 12\%$, and gradually increases.

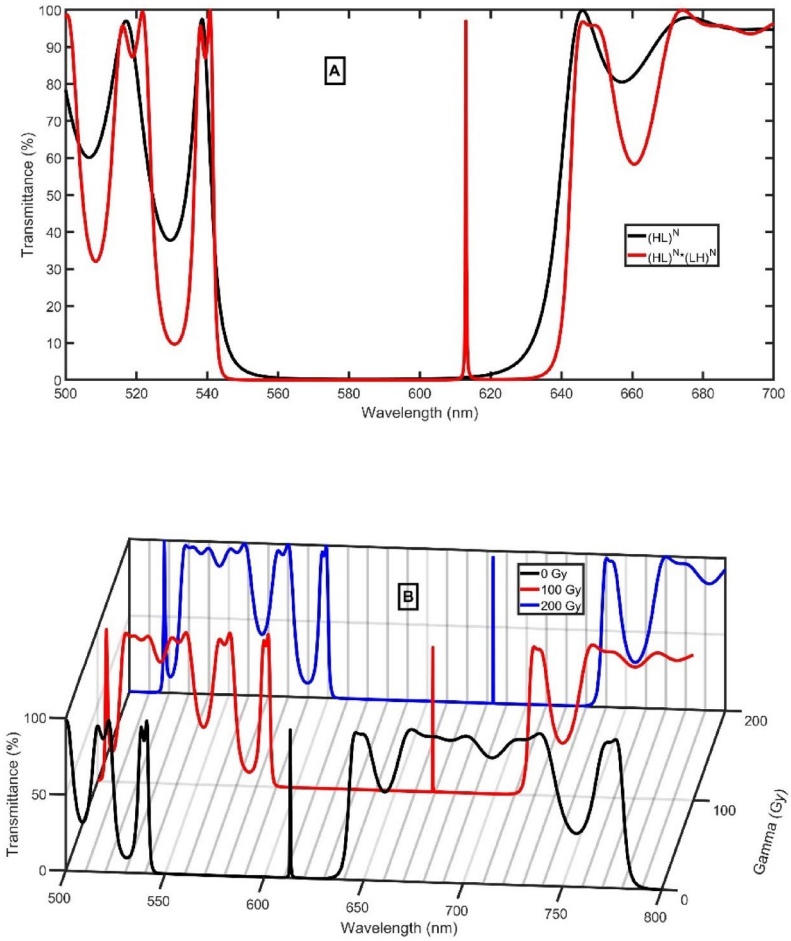

Fig. 3. Transmittance of (**A**) PhC1 (black line) and symmetrical structure of PhC1* PhC2 (red line) in the absence of gamma dose, and (**B**) Transmittance of symmetrical structure of PhC1* PhC2 at different gamma doses.

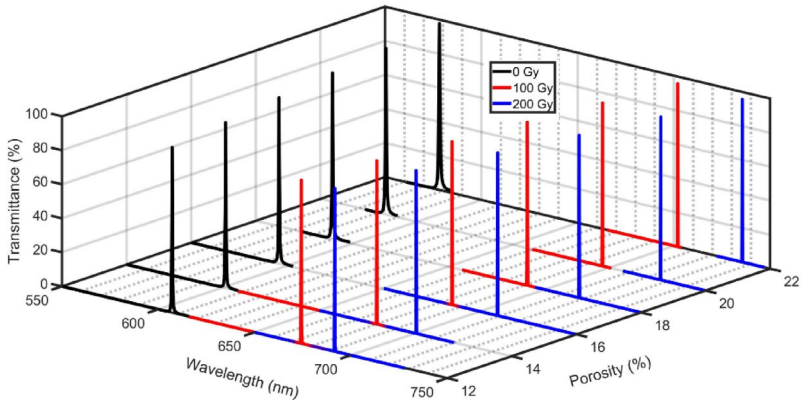

Fig. 4. Transmittance of symmetrical structure of PhC1* PhC2 at porosity of 12%,14%,, 16%, 18%, 20%, and 22% at different gamma doses (0 Gy in black spectrum, 100 Gy in red spectrum, and 200 Gy in blue spectrum).

Since increasing porosity negatively impacts the FWHM, N will be utilized to reduce FWHM and sharpen the edges of the PBG. As clear in Fig. 6, increasing N sharpens the left and right edges of the PBG. Besides, increasing N has a beneficial effect in reducing FWHM, keeping the transmittance constant, as clear in Fig. 7A. At a small number of cells (from 5 to 8 cells), the FWHM strongly decreases. Then, FWHM is slightly affected by N. Since increasing the number of cells has a slight effect on the peak position, the device's sensitivity remains

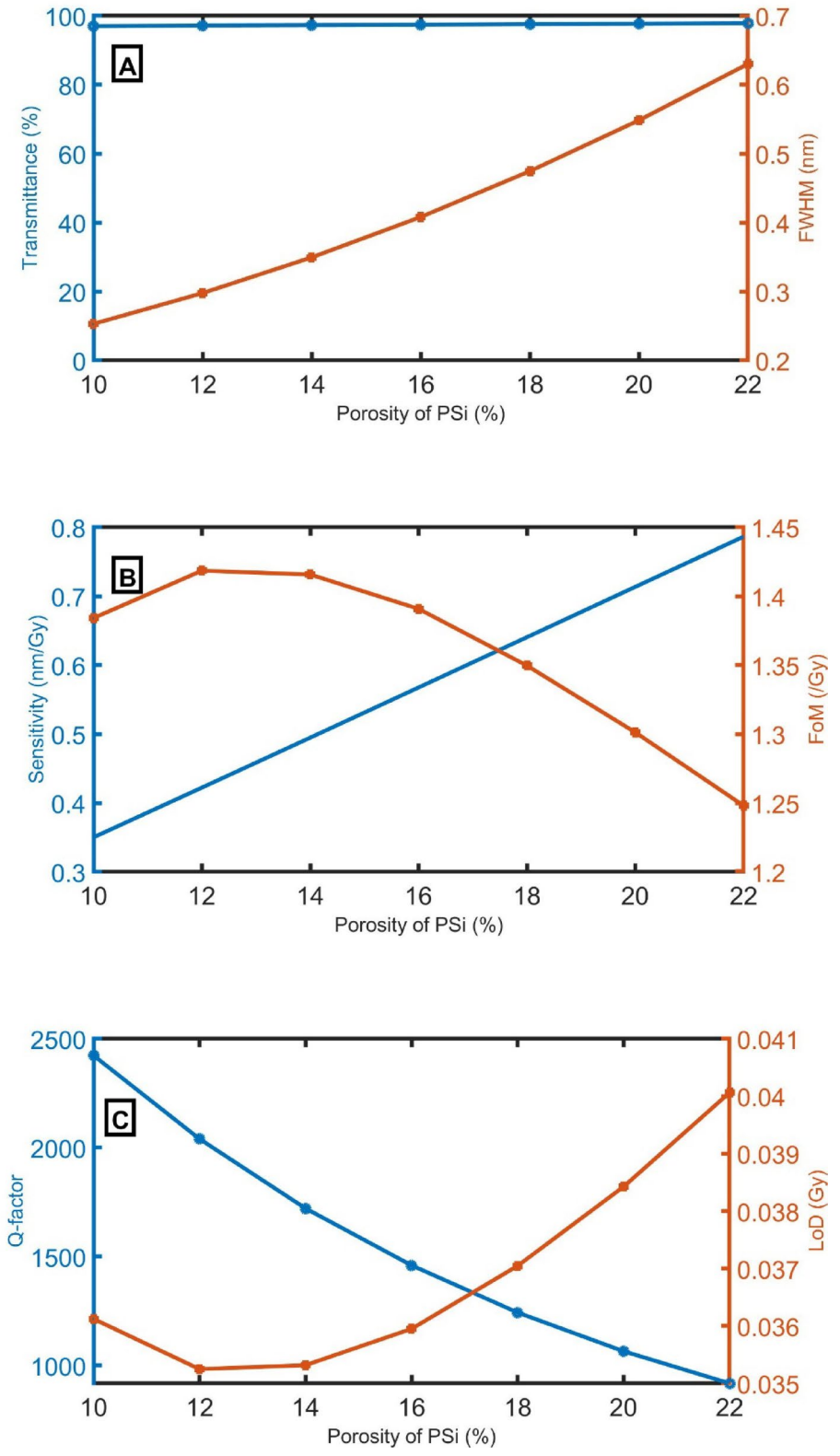

Fig. 5. (**A**) FWHM and transmittance at 0 Gy, (**B**) FoM and sensitivity, and (**C**) LoD and Q of the symmetrical structure of PhC1* PhC2 versus P of PSi layers.

unchanged. According to Eqs. (16–18) and Fig. 7B,C, FoM and Q enormously increase, and LoD gradually decreases.

By checking the transmittance of the outstanding peak versus N at 100 Gy and 200 Gy gamma dose, it is clear that changing the N from 5 to 7 periods has not affected the transmittance. The transmittance of the outstanding

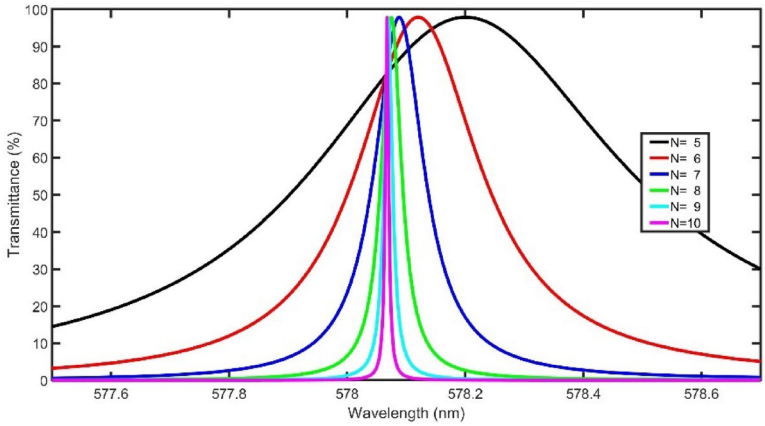

Fig. 6. Transmittance of the symmetrical structure of PhC1*PhC2 versus N at 0 Gy gamma dose.

peak is significantly and negatively impacted by increasing N from 7 to 10 periods, as clear in Fig. 8A,B). So, $N = 7$ cells for PhC1 and PhC2 is a suitable condition.

Using TES mode affects the position of the outstanding peaks because of the change in the complex RI of PSi. Figure 9 clears the variation of the outstanding peak position of the discussed detector for different gamma radiation doses after the optimization process. By increasing the gamma radiation doses from 0 to 100 Gy and 200 Gy, the outstanding peak position changed from 578.09 to 701.94 nm and 735.50 nm. From these results, one can infer that the analyzed structure is highly appropriate for the detection of gamma radiation doses from 0 to 200 Gy. Table 1 demonstrates that the proposed sensor exhibits greater sensitivity than others. This enhancement is due to this type of polymer, which is very sensitive to gamma doses compared to others[21]. Besides, the TES mode strongly depends on any change in the refractive index in any layer of the structure. As the PSi layer contains the PEONC, PEONC is very sensitive to gamma radiation; the TES mode is very sensitive to gamma radiation[48]. On the other hand, nonlinear response reduces accuracy and requires advanced calibration techniques to account for these deviations.

Conclusion

We presented the excitation of a TES in the visible EMW domain at the interface between 1DPhCs using the TMM theoretical approach as a gamma detector. By increasing the gamma irradiation doses, the RI of PEONC increased, the effective RI of PSi layers increased, and the position of the TES mode changed. As a result, the proposed structure recorded high sensitivity for gamma doses. The number of periods of PhC1 and PhC2 strongly affected the FWHM, FoM, Q-factor, and LoD. On the other hand, the ratio of PEONC in PSi strongly affected the sensitivity of the detector. The suggested detector has a supersensitivity for gamma doses from 0 to 100 Gy (1.24 nm/Gy) and high sensitivity for gamma doses from 100 to 200 Gy (0.34 nm/Gy). Finally, the proposed symmetrical structure performs exceptionally well in detecting gamma rays.

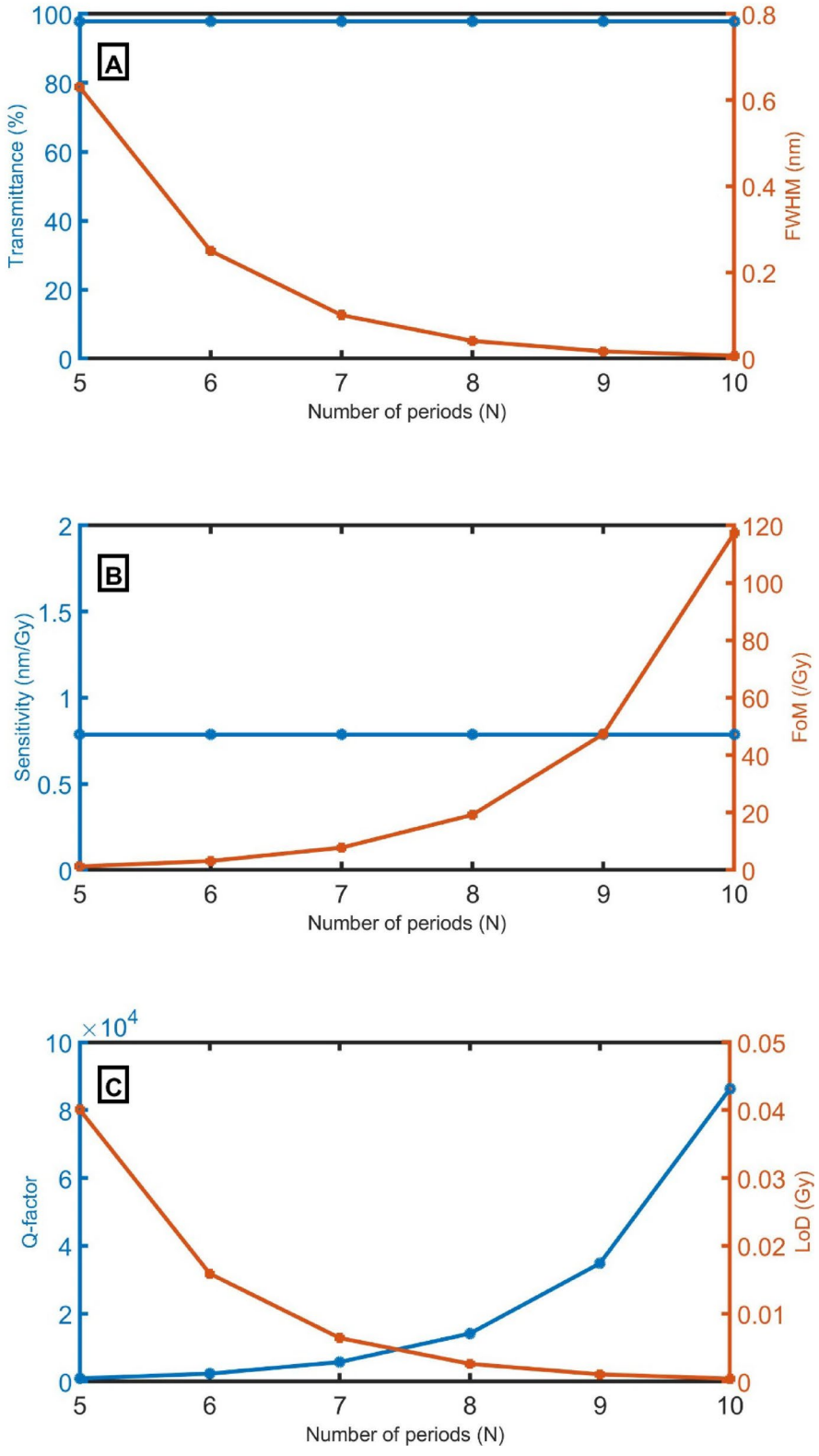

Fig. 7. (**A**) FWHM and transmittance at 0 Gy, (**B**) FoM and sensitivity, and (**C**) LoD and Q of the symmetrical structure of PhC1* PhC2 versus N.

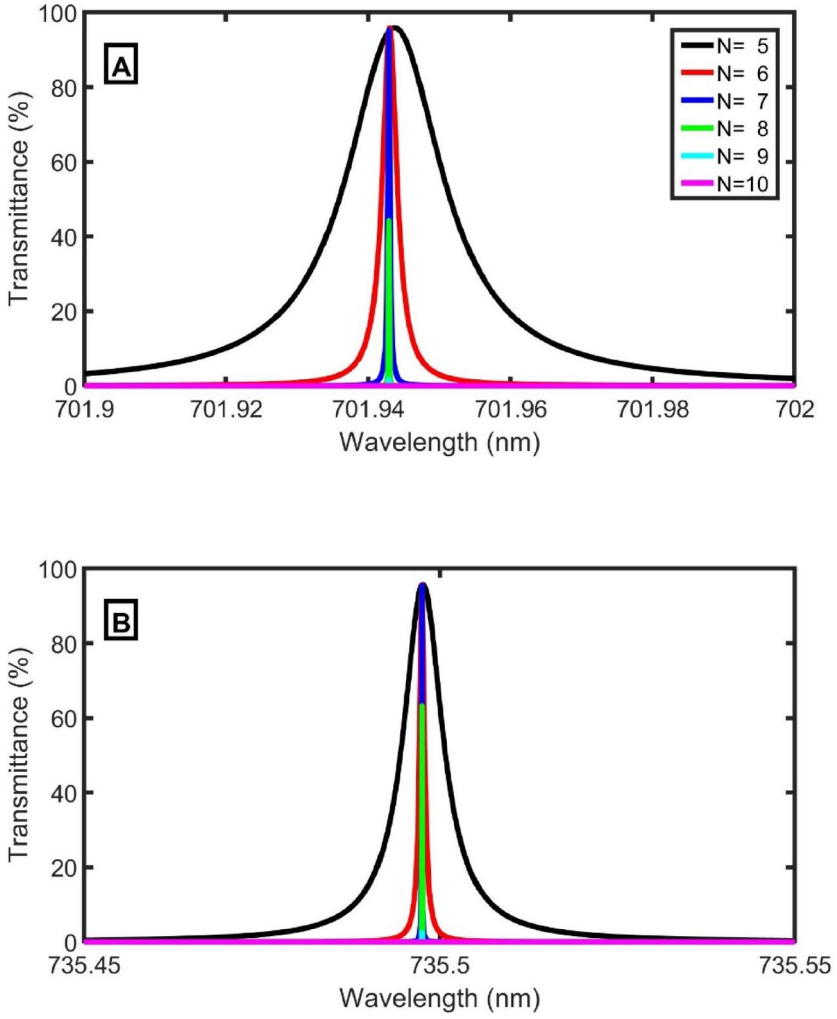

Fig. 8. Transmittance of the outstanding peak versus N at (**A**) 100 Gy and (**B**) 200 Gy gamma dose.

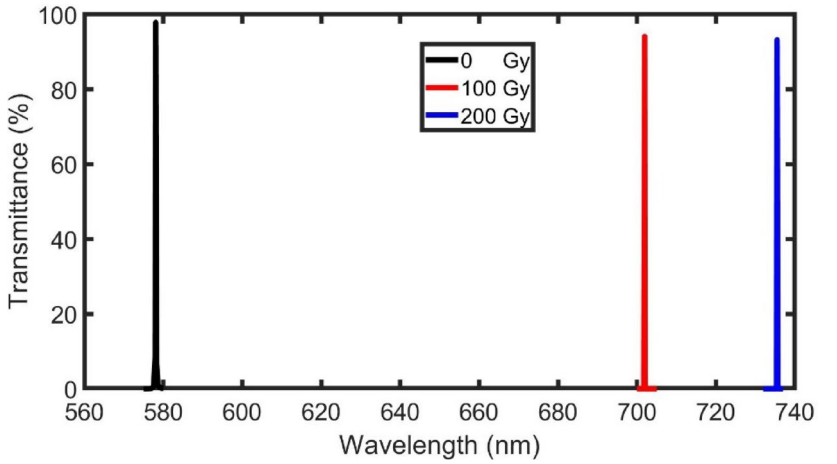

Fig. 9. Transmittance of the outstanding peaks at 0 Gy, 100 Gy and 200 Gy gamma dose.

References	S (nm/Gy)	Q	Range	Structure
2020,[65]	0.0013	NC	500 Gy	Fiber grating
2013,[27]	0.0002	NC	0–300 Gy	Indigo dye samples
2012,[66]	0.00018	NC	6000–65,000	Fiber grating
2018,[67]	0.0012	NC	0–500 Gy	Fiber grating
2024,[21]	0.265	12,701	0–70 Gy	1D-PC
2021,[68]	0.298	808	0–70 Gy	2D-PC
This work	1.24	1,970,000	0–100 Gy	TES-PC
This work	0.34	13,200,000	100–200 Gy	TES-PC

Table 1. Evaluating against various gamma radiation dose measurement devices.

Data availability

Requests for materials or code should be addressed to Zaky A. Zaky.

Received: 6 September 2024; Accepted: 13 May 2025
Published online: 22 May 2025

References

1. Butt, M., Khonina, S. & Kazanskiy, N. Recent advances in photonic crystal optical devices: A review. *Opt. Laser Technol.* **142**, 107265. https://doi.org/10.1016/j.optlastec.2021.107265 (2021).
2. Zaky, Z. A. et al. Photonic crystal with magnified resonant peak for biosensing applications. *Phys. Scr.* **98**, 055108. https://doi.org/10.1088/1402-4896/accbf1 (2023).
3. Butt, M. A., Khonina, S. N. & Kazanskiy, N. L. 2D-photonic crystal heterostructures for the realization of compact photonic devices. *Photonics Nanostruct. Fundam. Appl.* **44**, 100903. https://doi.org/10.1016/j.photonics.2021.100903 (2021).
4. Butt, M. A. & Khonina, S. N. Recent advances in photonic crystal and optical devices. *Crystals* **14**, 543. https://doi.org/10.3390/cryst14060543 (2024).
5. Zaky, Z. A. & Aly, A. H. Novel smart window using photonic crystal for energy saving. *Sci. Rep.* **12**, 10104. https://doi.org/10.1038/s41598-022-14196-9 (2022).
6. Zaky, Z. A., Al-Dossari, M., Zhaketov, V. & Aly, A. H. Defected photonic crystal as propylene glycol THz sensor using parity-time symmetry. *Sci. Rep.* **14**, 23209. https://doi.org/10.1038/s41598-024-73477-7 (2024).
7. Zaky, Z. A., Al-Dossari, M., Hendy, A. S. & Aly, A. H. Studying the impact of interface roughness on a layered photonic crystal as a sensor. *Phys. Scr.* **98**, 105527. https://doi.org/10.1088/1402-4896/acfa4a (2023).
8. Chowdhury, U., Mukherjee, R., Maity, A. R., Kumar, S. & Maji, P. S. Self-referenced refractive index sensor utilizing Tamm plasmon in a photonic quasicrystal. *Opt. Quant. Electron.* **55**, 869. https://doi.org/10.1007/s11082-023-05160-6 (2023).
9. Tammam, M. T., Zaky, Z. A., Sharma, A., Matar, Z. S., Aly, A. & Mohaseb, M. A. Defected photonic crystal array using porous GaN as malaria sensor. In *presented at the IOP Conference Series: Materials Science and Engineering* (2021). https://doi.org/10.1088/1757-899X/1171/1/012005
10. Gupta, A., Singh, T., Singh, R. K. & Tiwari, A. Numerical analysis of coronavirus detection using photonic crystal fibre-based SPR sensor. *Plasmonics* **25**, 1–9. https://doi.org/10.1007/s11468-022-01761-1 (2023).
11. Ivanov, I., Skryshevsky, V. & Belarouci, A. Chemical sensor based on the colorimetric response of porous silicon photonic crystal. *Sens. Actuators A* **333**, 113309. https://doi.org/10.1016/j.sna.2021.113309 (2022).
12. Yan, Q., Ma, R., Lyu, Q., Hu, X. & Gong, Q. Transmissible topological edge states based on Su–Schrieffer–Heeger photonic crystals with defect cavities. *Nanophotonics* **13**, 1397–1406. https://doi.org/10.1515/nanoph-2023-0744 (2024).
13. Li, C. et al. Thermo-optical tunable ultracompact chip-integrated 1D photonic topological insulator. *Adv. Opt. Mater.* **6**, 1701071. https://doi.org/10.1002/adom.201701071 (2018).
14. Raghu, S. & Haldane, F. D. M. Analogs of quantum-Hall-effect edge states in photonic crystals. *Phys. Rev. A—Atomic Mol. Opt. Phys.* **78**, 033834. https://doi.org/10.1103/PhysRevA.78.033834 (2008).
15. Sharifi, M., Rezaei, B., Pashaei Adl, H. & Zakerhamidi, M. S. Tunable Fano resonance in coupled topological one-dimensional photonic crystal heterostructure and defective photonic crystal. *J. Appl. Phys.* https://doi.org/10.1063/5.0135235 (2023).
16. Gao, W. et al. Fano-resonance in one-dimensional topological photonic crystal heterostructure. *Opt. Express* **26**, 8634–8644. https://doi.org/10.1364/OE.26.008634 (2018).
17. Ariza-Flores, A. D., Gaggero-Sager, L. & Agarwal, V. Effect of interface gradient on the optical properties of multilayered porous silicon photonic structures. *J. Phys. D Appl. Phys.* **44**, 155102. https://doi.org/10.1088/0022-3727/44/15/155102 (2011).
18. Huanca, D. R. One-dimensional porous silicon photonic crystals. In *Silicon Nanomaterials Sourcebook* 3–42 (CRC Press, 2017).
19. Kim, K., Lenshin, A., Chyragov, F. & Niftaliev, S. Formation of nanostructured tin oxide film on porous silicon. *Azerbaijan Chem. J.* **3**, 83–89 (2023).
20. Zaky, Z. A., Al-Dossari, M., Matar, Z. & Aly, A. H. Effect of geometrical and physical properties of cantor structure for gas sensing applications. *Synth. Met.* **291**, 117167. https://doi.org/10.1016/j.synthmet.2022.117167 (2022).
21. Zaky, Z. A., Al-Dossari, M., Hendy, A. S., Zayed, M. & Aly, A. H. Gamma radiation detector using Cantor quasi-periodic photonic crystal based on porous silicon doped with polymer. *Int. J. Mod. Phys. B* **38**, 2450409. https://doi.org/10.1142/S0217979224504095 (2024).
22. Hamsan, M., Shukur, M., Aziz, S. B., Yusof, Y. & Kadir, M. Influence of NH_4 NH_4 Br as an ionic source on the structural/electrical properties of dextran-based biopolymer electrolytes and EDLC application. *Bull. Mater. Sci.* **43**, 1–7. https://doi.org/10.1007/s12034-019-2008-9 (2020).
23. Aziz, S. B. et al. Effect of ohmic-drop on electrochemical performance of EDLC fabricated from PVA: Dextran: NH4I based polymer blend electrolytes. *J. Mater. Res. Technol.* **9**, 3734–3745. https://doi.org/10.1016/j.jmrt.2020.01.110 (2020).
24. Hamsan, M. et al. Solid-state double layer capacitors and protonic cell fabricated with dextran from Leuconostoc mesenteroides based green polymer electrolyte. *Mater. Chem. Phys.* **241**, 122290. https://doi.org/10.1016/j.matchemphys.2019.122290 (2020).
25. Aziz, S. B. et al. Fabrication of energy storage EDLC device based on CS: PEO polymer blend electrolytes with high Li+ ion transference number. *Results Phys.* **15**, 102584. https://doi.org/10.1016/j.rinp.2019.102584 (2019).
26. Qwasmeh, A. A. H. et al. Effects of gamma irradiation on optical properties of Poly (ethylene oxide) thin films doped with potassium iodide. *J. Compos. Sci.* **7**, 194. https://doi.org/10.3390/jcs7050194 (2023).

27. Bich, T., Mallam, S., Diso, D. & Hotoro, M. Determination of threshold radiation dose in the degradation process of indigo dye by gamma irradiation technique. *J. Phys. Sci. Innov.* **5**, 15–22 (2013).
28. Liu, C. et al. Transparent ultra-high-loading quantum dot/polymer nanocomposite monolith for gamma scintillation. *ACS Nano* **11**, 6422–6430. https://doi.org/10.1021/acsnano.7b02923 (2017).
29. Cai, W. et al. Synthesis of bulk-size transparent gadolinium oxide–polymer nanocomposites for gamma ray spectroscopy. *J. Mater. Chem. C* **1**, 1970–1976. https://doi.org/10.1039/C2TC00245K (2013).
30. Hosseini, M. A. et al. Dosimetric investigation of a new quantum dots/nanocomposite (CdTe QDs/PVK) sensor for real-time gamma radiation detection. *Appl. Phys. A* **125**, 1–8. https://doi.org/10.1007/s00339-019-3146-z (2019).
31. Esposito, F. et al. Optical properties of thin films monitored in real-time at high gamma radiation doses using long period fiber gratings. *Opt. Laser Technol.* **176**, 111019. https://doi.org/10.1016/j.optlastec.2024.111019 (2024).
32. Zaky, Z. A., Alamri, S., Zhaketov, V. & Aly, A. H. Refractive index sensor with magnified resonant signal. *Sci. Rep.* **12**, 13777. https://doi.org/10.1038/s41598-022-17676-0 (2022).
33. El-Shemy, S. et al. Radiation sensor based on a 1D-periodic structure infiltrated by (B-co-MP) a conjugated copolymer. *Sci. Rep.* **14**, 19829. https://doi.org/10.1038/s41598-024-65312-w (2024).
34. Ahmed, Z. et al. Assessing radiation hardness of silicon photonic sensors. *Sci. Rep.* **8**, 13007. https://doi.org/10.1038/s41598-018-31286-9 (2018).
35. Peng, S. et al. Three-dimensional single gyroid photonic crystals with a mid-infrared bandgap. *ACS Photonics* **3**, 1131–1137. https://doi.org/10.1021/acsphotonics.6b00293 (2016).
36. Min-Dianey, K. A. et al. Near-infrared transmissive properties of porous Si/Al_2O_3 photonic crystal band gaps. *Mater. Today Commun.* **33**, 104323. https://doi.org/10.1016/j.mtcomm.2022.104323 (2022).
37. Khalifa, M., Jaduaa, M. & Abd, A. Al_2O_3 NPs/porous silicon/silicon photovoltaic device. *J. Phys.: Conf. Ser.* https://doi.org/10.1088/1742-6596/1853/1/012046 (2021).
38. Tschikin, M., Ben-Abdallah, P. & Biehs, S.-A. Coherent thermal conductance of 1-D photonic crystals. *Phys. Lett. A* **376**, 3462–3465. https://doi.org/10.1016/j.physleta.2012.09.018 (2012).
39. Huang, Z. & Narimanov, E. E. Veselago lens by photonic hyper-crystals. *Appl. Phys. Lett.* https://doi.org/10.1063/1.4890276 (2014).
40. Seredin, P. et al. Ultrathin nano-sized Al_2O_3 strips on the surface of por-Si. *Mater. Sci. Semicond. Process.* **39**, 551–558. https://doi.org/10.1016/j.mssp.2015.05.067 (2015).
41. Perego, M. et al. Doping of silicon by phosphorus end-terminated polymers: Drive-in and activation of dopants. *J. Mater. Chem. C* **8**, 10229–10237. https://doi.org/10.1039/d0tc01856b (2020).
42. Sayed, F. A., Elsayed, H. A., Mehaney, A., Eissa, M. & Aly, A. H. A doped-polymer based porous silicon photonic crystal sensor for the detection of gamma-ray radiation. *RSC Adv.* **13**, 3123–3138. https://doi.org/10.1039/D2RA07637C (2023).
43. Du, Q. et al. Gamma radiation effects in amorphous silicon and silicon nitride photonic devices. *Opt. Lett.* **42**, 587–590. https://doi.org/10.1364/OL.42.000587 (2017).
44. Yeh, P. *Optical Waves in Layered Media* (Wiley, 1988).
45. Zaky, Z. A., Al-Dossari, M., Hendy, A. S., Badawy, W. M. & Aly, A. H. Periodic open and closed resonators as a biosensor using two computational methods. *Sci. Rep.* **14**, 11943. https://doi.org/10.1038/s41598-024-61987-3 (2024).
46. Zaky, Z. A. et al. Theoretical analysis of porous silicon one-dimensional photonic crystal doped with magnetized cold plasma for hazardous gases sensing applications. *Opt. Quant. Electron.* **55**, 584. https://doi.org/10.1007/s11082-023-04907-5 (2023).
47. Zaky, Z. A. et al. Theoretical optimization of Tamm plasmon polariton structure for pressure sensing applications. *Opt. Quant. Electron.* **55**, 738. https://doi.org/10.1007/s11082-023-05023-0 (2023).
48. Ameen, A. A., Al-Dossari, M., Zaky, Z. A. & Aly, A. H. Studying the effect of quantum dots and parity-time symmetry on the magnification of topological edge state peak as a pressure sensor. *Synth. Met.* **292**, 117233. https://doi.org/10.1016/j.synthmet.2022.117233 (2023).
49. Al-Dossari, M., Zaky, Z. A., Awasthi, S. K., Amer, H. A. & Aly, A. H. Detection of glucose concentrations in urine based on coupling of Tamm-Fano resonance in photonic crystals. *Opt. Quant. Electron.* **55**, 484. https://doi.org/10.1007/s11082-023-04621-2 (2023).
50. Zaky, Z. A., Al-Dossari, M., Sharma, A. & Aly, A. H. Effective pressure sensor using the parity-time symmetric photonic crystal. *Phys. Scr.* **98**, 035522. https://doi.org/10.1088/1402-4896/acbcae (2023).
51. El Malki, M., Khettabi, A., Sallah, M. & Zaky, Z. A. Noise filter using a periodic system of dual Helmholtz resonators. *Sci. Rep.* **14**, 24987. https://doi.org/10.1038/s41598-024-74799-2 (2024).
52. Zaky, Z. A., Al-Dossari, M., Sharma, A., Hendy, A. S. & Aly, A. H. Theoretical optimisation of a novel gas sensor using periodically closed resonators. *Sci. Rep.* **14**, 2462. https://doi.org/10.1038/s41598-024-52851-5 (2024).
53. Zaky, Z. A., Mohaseb, M. & Aly, A. H. Detection of hazardous greenhouse gases and chemicals with topological edge state using periodically arranged cross-sections. *Phys. Scr.* **98**, 065002. https://doi.org/10.1088/1402-4896/accedc (2023).
54. Zaky, Z. A., Mohaseb, M., Hendy, A. S. & Aly, A. H. Design of phononic crystal using open resonators as harmful gases sensor. *Sci. Rep.* **13**, 9346. https://doi.org/10.1038/s41598-023-36216-y (2023).
55. Zaky, Z. A., Alamri, S., Zohny, E. I. & Aly, A. H. Simulation study of gas sensor using periodic phononic crystal tubes to detect hazardous greenhouse gases. *Sci. Rep.* **12**, 21553. https://doi.org/10.1038/s41598-022-26079-0 (2022).
56. Zaky, Z. A., Singh, M. R. & Aly, A. H. Tamm resonance excited by different metals and graphene. *Photon. Nanostruct.-Fundam. Appl.* **49**, 100995 (2022).
57. Zaky, Z. A., Amer, H. A., Suthar, B. & Aly, A. H. Gas sensing applications using magnetized cold plasma multilayers. *Opt. Quant. Electron.* **54**, 217. https://doi.org/10.1007/s11082-022-03594-y (2022).
58. Zaky, Z. A., Al-Dossari, M., Zohny, E. I. & Aly, A. H. Refractive index sensor using Fibonacci sequence of gyroidal graphene and porous silicon based on Tamm plasmon polariton. *Opt. Quant. Electron.* **55**, 6. https://doi.org/10.1007/s11082-022-04262-x (2023).
59. Zaky, Z. A., Hanafy, H., Panda, A., Pukhrambam, P. D. & Aly, A. H. Design and analysis of gas sensor using tailorable Fano resonance by coupling between Tamm and defected mode resonance. *Plasmonics* **17**, 2103–2111. https://doi.org/10.1007/s11468-022-01699-4 (2022).
60. Wang, Z. et al. 1D partially oxidized porous silicon photonic crystal reflector for mid-infrared application. *J. Phys. D Appl. Phys.* **40**, 4482. https://doi.org/10.1088/0022-3727/40/15/016 (2007).
61. Ramirez-Gutierrez, C. F., Martinez-Hernandez, H. D., Lujan-Cabrera, I. A. & Rodriguez-García, M. E. Design, fabrication, and optical characterization of one-dimensional photonic crystals based on porous silicon assisted by in-situ photoacoustics. *Sci. Rep.* **9**, 1–15. https://doi.org/10.1038/s41598-019-51200-1 (2019).
62. Abdul-Kader, A. The optical band gap and surface free energy of polyethylene modified by electron beam irradiations. *J. Nucl. Mater.* **435**, 231–235. https://doi.org/10.1016/j.jnucmat.2013.01.287 (2013).
63. Abu Saleh, B. A., Elimat, Z. M., Alzubi, R. I., Juwhari, H. K. & Zihlif, A. M. Ultrafine iron particles/polystyrene composites: Effects of gamma radiation and manufacture aging on the AC electrical characterization. *Radiat. Effects Defects Solids* **177**, 1065–1074. https://doi.org/10.1080/10420150.2022.2105217 (2022).
64. Penn, D. R. Wave-number-dependent dielectric function of semiconductors. *Phys. Rev.* **128**, 2093. https://doi.org/10.1103/PhysRev.128.2093 (1962).
65. Esposito, F., Srivastava, A., Campopiano, S. & Iadicicco, A. Radiation effects on long period fiber gratings: A review. *Sensors* **20**, 2729. https://doi.org/10.3390/s20092729 (2020).

66. Kher, S., Chaubey, S., Kashyap, R. & Oak, S. M. Turnaround-point long-period fiber gratings (TAP-LPGs) as high-radiation-dose sensors. *IEEE Photonics Technol. Lett.* **24**, 742–744. https://doi.org/10.1109/LPT.2012.2187637 (2012).
67. Stăncălie, A. et al. Long period gratings in unconventional fibers for possible use as radiation dosimeter in high-dose applications. *Sens. Actuators A* **271**, 223–229. https://doi.org/10.1016/j.sna.2018.01.034 (2018).
68. Ibrahim, M. S. S., Hamed, M. K. G., El-Okr, M. M., Obayya, S. & Hameed, M. F. O. Highly sensitive photonic crystal gamma ray dosimeter. *Opt. Quant. Electron.* **53**, 348. https://doi.org/10.1007/s11082-021-02968-y (2021).

Acknowledgements

The authors are thankful to the Deanship of Graduate Studies and Scientific Research at University of Bisha for supporting this work through the Fast-Track Research Support Program. The authors acknowledge the joint project between the Academy of scientific research and technology (Egypt) and the Joint Institute for Nuclear Research (Dubna—Russia) ASRT-JINR collaboration (ID: JINR Research Project_202324646).

Author contributions

Z.A. Zaky invented the original idea of the study, implemented the computer code, performed the numerical simulations, analyzed the data, wrote and revised the main manuscript text, and was the team leader. M. Sallah analyzed the data and discussed the results. V. D. Zhaketov analyzed the data and discussed the results. A. H. Aly analyzed the data and discussed the results. Finally, all Authors developed the final manuscript.

Funding

The is no fund.

Declarations

Competing interests

The authors declare no competing interests.

Additional information

Correspondence and requests for materials should be addressed to Z.A.Z.

Reprints and permissions information is available at www.nature.com/reprints.

Publisher's note Springer Nature remains neutral with regard to jurisdictional claims in published maps and institutional affiliations.